

Dynamics of crystallization in hard-sphere suspensions

Yueming He and Bruce J. Ackerson

Department of Physics and Center for Laser Research, Oklahoma State University, Stillwater, Oklahoma 74078-0444

W. van Meegen and S. M. Underwood

Department of Applied Physics, Royal Melbourne Institute of Technology, Melbourne, Victoria, Australia

Klaus Schätzel*

Institut für Physik, Johannes Gutenberg Universität, D-55099 Mainz, Germany

(Received 22 December 1994; revised manuscript received 11 December 1995)

Density fluctuations are monitored by small-angle light scattering during the crystallization of 0.22- μm -radius, hard colloidal spheres. Measured structure factors show an intensity maximum at finite-scattering vectors. The shape of the intensity distribution scales at early times during nucleation and growth and again at large times during ripening. At intermediate times there is a crossover region where scaling ceases to be valid. Both the amplitude and the position of the maximum intensity show quasi-power law behavior in time. The values of the observed exponents are within the range expected for classical growth models. The breadth of the intensity distribution increases with increasing volume fraction, suggesting greater crystal polydispersity with increasing volume fraction. The lower volume fraction intensity distributions suggest that crystals have a compound or internal structure, while the observed decrease in characteristic length in the crossover time regime may indicate breakup of crystals to this smaller internal structure. The results of measurements are compared with results calculated for nucleation and growth of crystals in suspensions of hard spheres. Results also are compared with earlier measurements made on samples containing 0.50- μm radius spheres. Differences in the two systems are discussed in terms of interparticle potential, polydispersity, and gravitational effects. [S1063-651X(96)09610-9]

PACS number(s): 64.70.Dv, 81.10.Fq, 82.70.Dd

I. INTRODUCTION

The dynamics of crystallization, the disorder-to-order transition from a metastable fluid to a crystalline solid, is very rapid and difficult to characterize in simple atomic systems. Only recently have advances in instrumentation permitted kinetic studies of crystallization in metallic glasses by using x-ray diffraction with millisecond time resolution [1]. In complex fluids crystallization dynamics is orders of magnitude slower and the lattice constants are on the order of the wavelength of light. Thus time-resolved optical analogues of x-ray diffraction [2–6] and microscopy [7] have proved useful in characterizing homogeneous nucleation and growth in these systems.

In colloidal systems the suspended particles order into crystalline lattices from initially shear melted [8] amorphous metastable fluid states. These samples differ from pure atomic systems in that the sample volume is fixed by the suspending fluid, and crystallization occurs at fixed volume rather than fixed pressure. Furthermore, the particles exchange energy and momentum with the solvent. Any latent heat produced is rapidly dissipated by the solvent with negligible change in temperature. Finally, the colloidal particle interactions are essentially repulsive due to charge stabilization or steric stabilization to prevent particle aggregation. Despite these differences between atomic and colloidal systems, we expect the essential features of the phase transition to be similar in atomic and complex fluid systems.

Most homogeneous colloidal crystallization work has focused on the crystal order parameter, a nonconserved parameter used to characterize the disorder-to-order phase transition. Aastuen *et al.* [2] have made direct observations of growing crystallites in aqueous suspensions of charge stabilized polystyrene spheres as a function of particle volume fraction. The size of the crystals was found to be directly proportional to the elapsed time, indicating interface-limited growth. The velocity increased and saturated with increased sample volume fraction and was characterized by the classical Wilson-Frenkel growth law. Dhont *et al.* [4] used time-resolved light scattering to monitor the first-order Bragg peak during crystallization in suspensions of slightly charged silica particles. Interface-limited growth was assumed implicitly and a classical analysis made to determine induction times, nucleation and growth rates, and the sizes and numbers of the crystals as a function of particle volume fraction. The nucleation rate density was found to have a much weaker dependence on volume fraction than predicted [9].

Recently a conserved parameter, the particle density, has been monitored during the crystallization process [5,6,10]. Small-angle light-scattering (SALS) measurements were made during the crystallization process in suspensions of sterically stabilized spheres in a solvent that has nearly the same index of refraction as the particles. The observed scattered intensity distribution had a maximum at finite-scattered wave vector and was observed to scale over nearly the full observation time. As a result, the experimental data were represented by the position and magnitude of the intensity maximum as a function of time. Two distinct time regimes were observed and termed “nucleation and growth” and

*Deceased.

“ripening.” In the nucleation and growth region the intensity maxima were observed to follow a power-law increase in time with an exponent of 4 for volume fractions equal to or less than the melting value. Similarly the position of the maximum moved towards zero scattering angle with increasing time, following an inverse square-root time dependence near melting volume fractions. Thus a characteristic length was increasing as the square root of time and was consistent with diffusion-limited rather than interface-limited growth. The intensity growth exponent was explained in terms of a constant nucleation rate and the diffusion-limited growth of crystals.

In the ripening region, the growth of the maximum intensity was much slower with an exponent of unity or less. The exponent for the position of the maximum was one-third for volume fractions less than the melting value. This is consistent with the exponent for Ostwald ripening in a two-phase region. For volume fractions greater than melting the exponent was observed to be one-half, consistent with the exponent for growth through domain-wall motion. Dynamical scaling was also examined and found to give the expected scaling exponent of 3 for this three-dimensional system for volume fractions equal to the melting value or less. For larger volume fractions, the exponent was observed to be 2 and is not yet understood.

In this work we present results of similar small-angle light experiments for suspensions of smaller radii colloidal particles. A number of samples closely spaced in volume fraction were studied. The growth exponents for both the intensity and the characteristic length were larger than those found at corresponding volume fractions for the previously studied 0.50- μm -radii particles. All samples exhibited a decrease in scattered intensity and reduction in characteristic length in the crossover region between nucleation-and-growth and ripening. This combined with changes observed in the shape of the small-angle intensity distribution suggest crystal breakup or dissolution in the crossover region before ripening commences. The intensity distribution shape functions became broader as the volume fraction of particles increased. This is attributed to a larger polydispersity of the scattering entities with increasing volume fraction.

In Sec. II the samples, experimental apparatus, and procedure are discussed. This is followed by a presentation of the results. Finally we compare the data with theory for classical crystallization in suspensions of hard spheres and with measurements taken for suspensions with larger radii spheres. The differences are discussed in terms of interparticle potential, polydispersity, and gravitational effects.

II. EXPERIMENT

A. Particles

The colloidal suspensions used in these experiments contained uniformly sized polymethylmethacrylate (PMMA) spheres coated with a thin (~ 10 -nm) layer of poly-12-hydroxystearic acid [11]. This coating provided sufficient steric stabilization to prevent flocculation. The particle radius was determined to be 215 nm with a polydispersity of 7% relative standard deviation by dynamic light scattering on diluted suspensions. The solvent was a mixture of tetralin (46 wt %) and decalin (54 wt %) in a ratio adjusted to closely

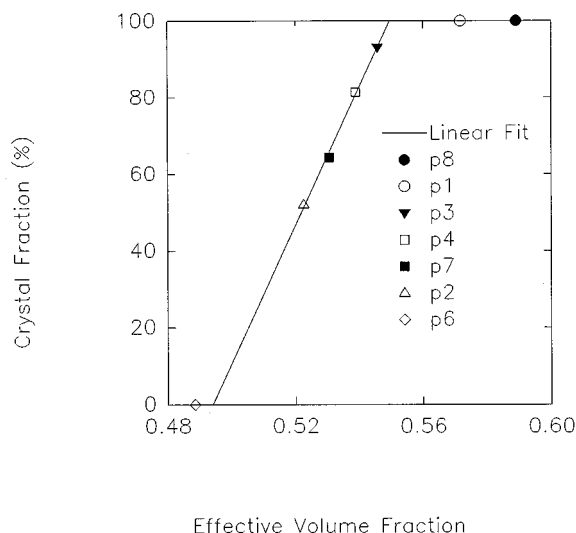


FIG. 1. Phase diagram for the colloidal system used in the experiment. The freezing point is fixed at 0.494, as described in the text, and a fit determines the melting point to be a volume fraction of 0.55.

match the index of refraction of the suspended particles. Exact matching was not possible due to the difference in the refractive index of the particle core and coating. Also, the matching point is sensitive to temperature and probing wavelength. However, samples with particle volume fractions on the order of 50% appeared clear to the eye and showed a total scattering of less than 50% of the incident light for a path length of 10 mm at a wavelength of 633 nm. The losses were due primarily to small-angle and Bragg scattering.

Samples having different particle concentrations were prepared by loading optical quality cuvettes (10 mm \times 10 mm \times 50 mm) with an index-matched stock sample of known weight of each solvent and particle component. The particles were then centrifuged to the bottom of each cuvette, and different weights of the supernatant were withdrawn to obtain a series of samples having particle weight fractions ϕ_w ranging from 0.391 to 0.491. The particles were redispersed by vigorous agitation of the cuvettes, which were then left undisturbed for approximately two months. During this time crystallization commenced and the crystals that were more dense than the amorphous phase settled. The phase diagram shown in Fig. 1 was determined using the sedimentation tracking method of Paulin and Ackerson [12]. The volume fraction $\phi = (0.494/0.395)\phi_w$ has been rescaled from the weight fraction to make the freezing point coincide with the value for hard spheres, $\phi_f = 0.494$ [13]. It is seen that this rescaling brings the melting point $\phi_m = 0.55 \pm 0.01$ into close agreement with that for hard spheres (0.545 ± 0.02). The required rescaling was larger than that for PMMA particles having twice the radius [12] but was the same order as that required for similar sized particles (325 nm in radius) suspended in mixtures of decalin and CS_2 [14]. It is believed that absorption of tetralin or CS_2 into the particle coating (or core) may be responsible for this effect [14–16]. The weight of each cuvette was monitored to account for any change in particle volume fraction due to solvent evaporation over the duration of these experiments.

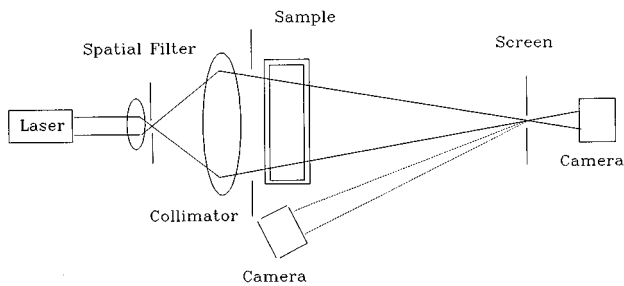


FIG. 2. Optical setup used for small-angle light-scattering. The different camera positions correspond to transmission and reflection geometries. The transmission geometry setup has six times the intensity of the reflection geometry.

B. Small-angle light-scattering setup

The small-angle light-scattering setup shown in Fig. 2 was modified slightly for some measurements from that reported previously [6]. A small HeNe laser beam (5 mW, polarized) was spatially filtered and expanded using a microscope objective (20 \times) and a pin hole (25- μ m-diameter) in a commercial mechanical (Newport) unit. A single "best form" lens ($f=80$ mm, antireflection coated for 633 nm) refocused the filtered beam onto the detection screen. An aperture adjusted to coincide with the first diffraction minimum (~ 9 mm) produced by the pinhole was placed just before the sample. Careful aperture adjustment minimized diffraction both from the aperture and from scattering by sample cell walls. The detection screen was adjusted to lie between 0.68 and 1.25 m from the sample. The distance chosen depended on the particular sample.

Scattered light was detected in either a transmission or reflection geometry. In the reflection geometry used previously [6], the focused primary beam passed through a 2–5 mm hole in the center of the screen to a distant beam stop. The smaller hole sizes were needed for the relatively smaller scattering patterns produced by larger crystals of the lower volume fraction samples. Scattered light was detected by a charge-coupled-device (CCD) video camera placed slightly off axis, typically just below the main beam and close to the sample. In the transmission geometry the primary beam was incident on a beam stop placed directly on the detection screen. The CCD video camera was placed on axis with the beam a distance of 60 cm behind the detection screen.

Measurements in either geometry gave identical results, except that the magnitude of the scattered light was approximately sixfold larger in the transmission geometry. This larger intensity proved useful for the relatively weak scattering produced by the larger volume fraction samples. These two arrangements kept the geometric distortions negligible for the observed small-angle scattering. The camera resolved 192 by 165 pixels, and exposure times were kept close to 200 ms. The scale of the scattering wave vector $q=4\pi n\sin(\theta/2)/\lambda$ was calibrated by placing a grating with 200 lines/in. in the position of the sample and detecting the positions of the diffracted maxima using two orthogonal orientations of the grating. Here the index of refraction of the solvent is given by n , the incident laser wavelength by λ , and the scattering angle by θ .

C. Data analysis

Data analysis followed the same procedure developed previously [6]. The CCD video camera was driven by a per-

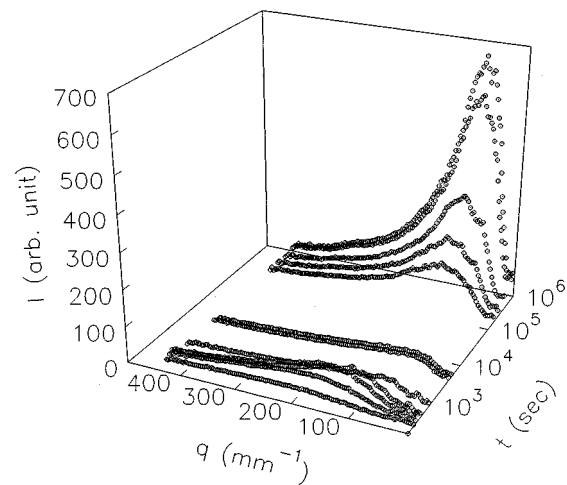


FIG. 3. Measured light scattering intensity as a function of scattering vector and time for sample p3 ($\phi=0.549$). Three distinct regions are observed: nucleation and growth ($t<510$ sec), cross-over ($510<t<192000$ sec), and ripening ($t>192000$ sec).

sonal computer that accepted the digitized image data having 8-bit resolution and stored the data on magnetic disks. Frame rates varied from one frame every 20 sec (immediately after shear melting) to one every hour at large times. At the end of a data collection run, the processing involved careful centering of the series of scattering images followed by the calculation of radial intensity distributions $I(q)$.

To eliminate detector dark count, low angle static scattering produced by the sample cuvette, and a small amount of residual static scattering from the optical system, a radial intensity distribution from an early image was subtracted from each of the other intensity distributions. Typically the chosen image exhibited the smallest intensity values throughout the useful q range. In most cases all early images were almost equivalent. However, index-of-refraction changes, associated with temperature equilibration or sample flow relaxation after shear melting, can produce scattering changes in this time range and must be avoided. The temperature of the samples was maintained to within $\pm 1^\circ\text{C}$. After compensating for differences in optical setup, apertures, and exposure times, all intensities can be represented approximately on the same scale. Because the smaller particle samples studied here exhibit nucleation and growth on a faster time scale than the previously reported samples with larger radii particles, faster initial frame rates were required to obtain image data suitable for subtraction.

Background-subtracted intensity distributions evidenced a ring structure with a maximum in the intensity at finite wave vector q_m . The value of the maximum and its position changed with time, as shown in Fig. 3. The value of the maximum I_m was determined by fitting a second-order polynomial to the data in a limited region around the peak. The ring position could be characterized most accurately by the larger wave vector $q_{1/2}$, where the intensity distribution fell to half its maximum value. I_m and $q_{1/2}$ were studied as functions of time and also used to obtain scaled structure factors as follows:

$$S(Q,t)=I(q,t)/I(q_m,t), \quad Q=q/q_{1/2}(t). \quad (1)$$

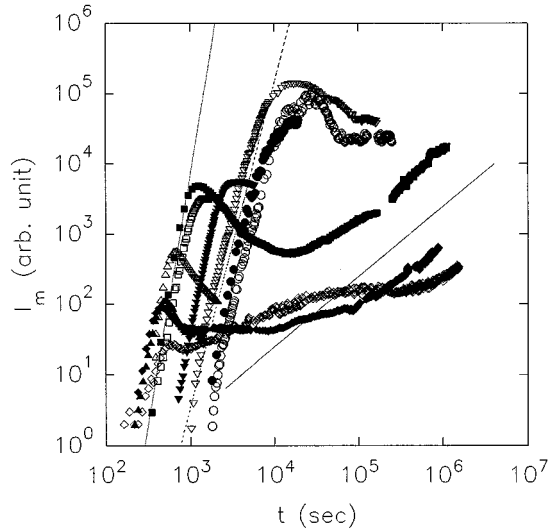


FIG. 4. Peak intensity $I_m(t)$ as a function of time for different volume fraction samples. Power laws t^7 (dotted line), $t^{4.5}$ (dashed line) in the early time region, and t^1 (solid line) in the late time region are indicated.

III. RESULTS

A. Time dependence

Figures 4 and 5 show, respectively, the parameters I_m and $q_{1/2}$ for the intensity maximum and location as a function of time elapsed since the cessation of shear melting. The double logarithmic scales demonstrate the large dynamic range of the data and any approximate power-law growth behavior. For all samples the I_m show the same qualitative form. There is an initial rapid growth to a maximum value followed by a decrease to a lower value. When runs are made to sufficiently large elapsed times, I_m again evidences an increase in value. For purposes of discussion we will consider this behavior to consist of three parts, as done in previous studies [6]: (1) an “initial nucleation and growth” region from zero time to the time where the maximum in scattered intensity I_m occurs, (2) a “crossover” region from the time of the first maximum to approximately the point where I_m begins the second increase in value, and (3) the “ripening” region where the large elapsed time increase in I_m occurs. Any breaks in these intensity data correspond with adjustments in the beam intensity to avoid saturating the CCD video camera as the scattered intensity increases. The symbols correspond to those in Fig. 7.

In the nucleation and growth regions, I_m exhibits nearly power-law growth in elapsed time with an exponent 4.66 ± 0.02 ($\phi = 0.531$) at one of the lowest volume fractions and increasing to a maximum value of 7.15 ± 0.16 ($\phi = 0.545$) before decreasing to 5.57 ± 0.23 ($\phi = 0.549$) for a sample near melting and further decreasing to 3.6 ± 0.1 ($\phi = 0.551$) for the fully crystallized sample. At the larger volume fractions, I_m remains fairly constant for a large range of elapsed time (two days) in the crossover region, while at the lower volume fraction measured, I_m is not constant for a similar range of crossover time. In the ripening region the data at the largest measured elapsed times may be characterized by linear or sublinear power-law behavior. The quoted

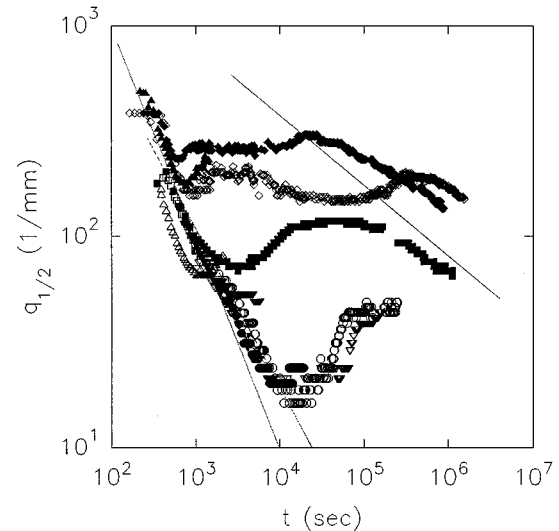


FIG. 5. Characteristic scattering vector $q_{1/2}(t)$ as a function of time for different volume fraction samples. Power laws $t^{-0.75}$ for low concentration samples (dotted line), and t^{-1} for samples near the melting point (dash line) in the early time region and $t^{-1/3}$ (solid line) in the late time region are indicated.

error in the exponential values is determined from the best fit to the data.

In Fig. 5, $q_{1/2}$ is shown as a function of elapsed time, where it is seen that all volume fractions appear to have the same qualitative behavior. The characteristic wave vector initially decreases in magnitude, indicating the growth of a characteristic length. However, this wave vector evidences a minimum and then increases with increasing elapsed time. This implies a decrease in the characteristic length in this elapsed time region. At sufficiently large elapsed times, the characteristic wave vector again decreases, indicating a growth of the characteristic length. Like the I_m data, these data may be discussed in terms of three regions. The initial growth of a characteristic length scale corresponds to a nucleation and growth region. The time where the characteristic length scale decreases to the time where it again increases corresponds to a crossover region. A ripening region corresponds to the large elapsed times where the characteristic length scale increases. This identification is somewhat ambiguous, since the I_m maximum and the $q_{1/2}$ minimum do not occur at exactly the same time, the minimum being later in time. With this discrepancy in mind we will use this terminology (nucleation and growth, crossover, and ripening) to discuss the time-dependent data.

In the nucleation and growth region $q_{1/2}$ decreases with an approximate power-law behavior ranging from 0.75 ± 0.02 ($\phi = 0.531$) at the smallest volume fraction measured to 1.01 ± 0.08 ($\phi = 0.549$) for the sample near the melting point. In the crossover region the characteristic length remains fairly constant, as does the intensity for the larger volume fractions. For the lower volume fractions the characteristic length changes, as does the intensity. For the largest elapsed times we compare the data with decreasing power-law exponent of $1/3$. While the data approximate this power-law behavior, it is not clear if this is the ultimate asymptotic behavior of the data. Measurements at even larger elapsed

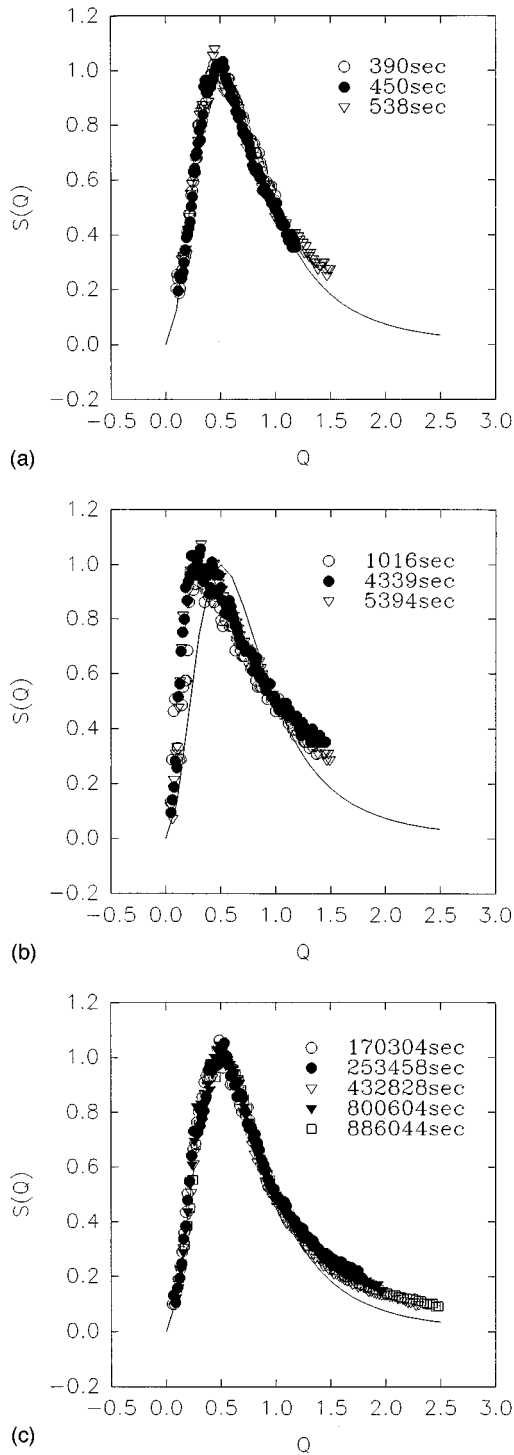


FIG. 6. Structure factors for data in Fig. 3 in three time regions, “nucleation and growth” (a), “crossover” (b), and “ripening” (c). Time regions are shown, as well as the Furukawa scaling function $F(Q)$ (line) as a guide to the eye.

times would require better temperature control and laser stability.

B. Scaling

The normalized or scaled structure factor is shown in Fig. 6 using the data in Fig. 3 for a sample near the melting point ($\phi=0.549$). From these data we conclude that the scattered

intensity does not scale over the full time domain, because it cannot be completely characterized by $I_m, q_{1/2}$ and a single shape function. However, the scaling is punctuated. For limited time regions, scaling is observed to hold. These regions correspond to the initial nucleation and growth phase for times less than 600 sec and to the ripening phase for times greater than 150 000 sec. Despite the great time lapse separating the two regions, the shape function indicated by the solid lines in Fig. 6 is very similar. The crossover region is much less settled where the shape function, being much broader, deviates markedly from that observed in the other two regions. Furthermore, it changes rapidly to this form, which shows approximate scaling in the time range between 600 and 6000 sec, but evolves slowly at larger elapsed times to the ripening form.

The shape functions also depend on the volume fraction, as shown in Fig. 7. A double logarithmic plot of $S(Q)$ is given as a function of Q and parametrized by volume fraction. The shape function for each volume fraction is shifted by an order of magnitude from the neighboring ones for clarity of presentation. As the volume fraction decreases, the scattered intensity maximum moves to smaller angles and cannot be resolved reliably with our apparatus for volume fractions less than 0.525. As the volume fraction increases, the shape function broadens in all scaling time domains. To make more quantitative comparisons the data have been fitted by the Furukawa form [17]

$$S(Q, \phi) = \frac{[1 + \gamma(\phi)/2]Q'^2}{\gamma(\phi)/2 + Q'^{2+\gamma(\phi)}}, \quad (2)$$

where

$$Q' = f(\phi)Q. \quad (3)$$

Here the exponent $\gamma(\phi)$ and the scale parameter $f(\phi)$ are fitting parameters that depend on volume fraction. Table I presents values for $\gamma(\phi)$, and values for $f(\phi)$ are redundant since they are a result of the definition of $q_{1/2}$ not being at the intensity maximum. Due to solvent evaporation during the duration of these experiments a given sample could be used to obtain data at several different volume fractions, and these are included in Table I. The form of Eq. (2) is quadratic in the small Q' limit. The data in the nucleation and growth region, where small Q' data is most accessible, are reasonably consistent with this form. In the ripening region the larger characteristic lengths make this region less accessible. For the larger volume fraction samples measured, the Furukawa form gives a reasonable fit to the data for the full Q' range. However, at the lower volume fractions, there is a more complicated large Q' asymptotic dependence, which may be constructed from two power-law decays with different exponents. In Table I values of $\gamma(\phi)$ are given for a fit that neglects the large Q' asymptotic behavior and a result in parenthesis that fits to the large Q' values. For the smaller volume fraction sample ($\phi=0.539$) we see an evolution from the complex decay behavior in the nucleation and growth region at large Q' values to a single power-law decay in the ripening region. We do not want to argue any general significance for using the Furukawa form (and, in fact, the exponents are far different from those usually found in

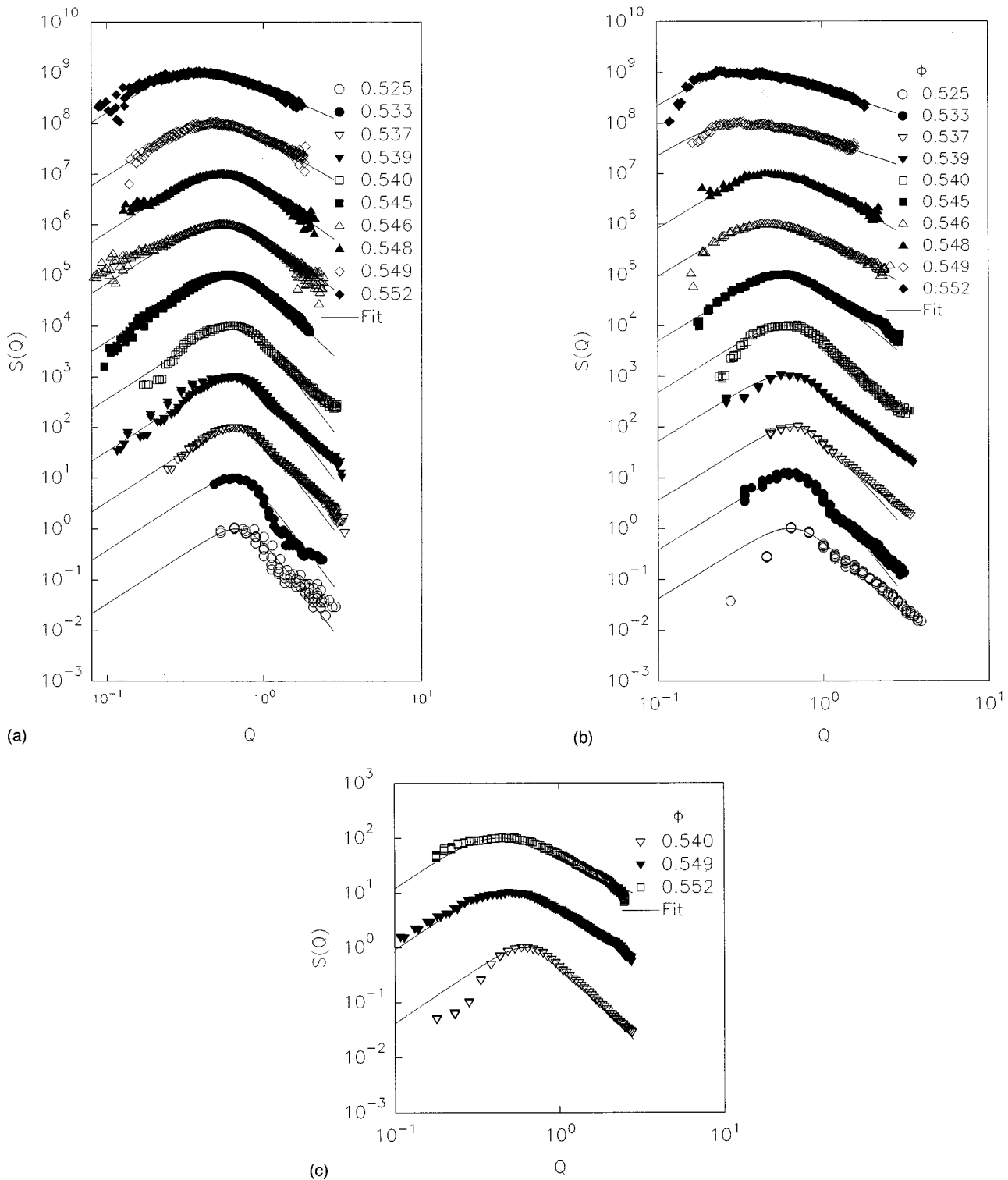


FIG. 7. Structure factors for various volume fraction samples in three time regions, “nucleation and growth” (a), “crossover” (b), and “ripening” (c) time regions, and Furukawa scaling function $F(Q)$ (line). For clarity each data set is shifted by an order of magnitude from the neighboring curves. Note the lack of fit with the Furukawa form for the lower volume fraction samples at large scattered wave vector.

liquid-gas and fluid demixing transitions), but we find it a convenient form to fit the data.

IV. DISCUSSION

The motivation for this work was to check previous results with a different system, to expand the scattering vector

space available to our apparatus by effectively reducing the crystal size, to reduce the effects of sedimentation by using smaller-size particles, and to expand the range of volume fractions studied. However, measurements at large volume fractions were ultimately limited by diminished sample scattering with either size particles. At smaller volume fractions, crystallite sizes typically were larger for the smaller-particle

TABLE I. The values in Eq. (2) corresponding to various volume fractions for different samples in three time regions.

Sample	p_2	p_7	p_7	p_4	p_4	p_4	p_4	p_3	p_3	p_3
ϕ	0.525	0.533	0.537	0.539	0.540	0.545	0.546	0.548	0.549	0.552
Nucl. and growth region	4.0	4.1	4.0(3.4)	4.0(3.5)	4.0(3.0)	2.9	2.2	2.2	1.8	1.3
Crossover region	3.1	3.7	3.6	2.8	3.0	2.75	1.8	1.9	1.1	1.1
Ripening region				2.9				1.82	1.53	

systems and confounded our attempts to improve apparatus resolution. The region between nucleation–growth and ripening, the ‘‘crossover region,’’ became more pronounced for the smaller-particle samples and limited our ability to study ripening compared to the larger-particle systems. We now make more explicit these differences with earlier work and offer explanations in terms of possible deviations from hard-sphere behavior, sample polydispersity, and gravitational effects.

A. Comparison with previous hard-sphere studies

The data presented here for 0.22- μm -radius particle samples extend and contrast with the earlier small-angle light-scattering studies made for suspensions containing 0.50- μm -radius particles [6]. Other than the differences in particle radius, the same solvents, PMMA particle cores, and steric stabilizers are used in both of these sample systems. Numerous studies on both systems indicate that they approximate suspensions of hard colloidal spheres [12,14–16]. Qualitatively, the crystallization process is similar. After cessation of shear melting, there is a rapid increase in the intensity of forward-scattered light. The intensity distribution is in the shape of a ring that exhibits scaling and collapses in size during the ‘‘nucleation and growth’’ phase. There is a ‘‘crossover’’ region followed by a ‘‘ripening’’ phase. The shape function in the nucleation and growth region is found to be similar to that in the ripening region for the larger volume fraction samples.

A comparison of the two different radii samples is given in Fig. 8. The reduced elapsed time $\tau_c = D_0 t_c / a^2$ taken to reach the maximum intensity I_m (beginning of the crossover region) is shown in Fig. 8(a) as a function of volume fraction. Here a is the particle radius, D_0 is the dilute-solution particle diffusion constant, and t_c is the elapsed time to the maximum in I_m . The reduced wave vector $q_{\min} a$ at the beginning of the crossover region is a local minimum for the smaller radii particles and is shown as a function of volume fraction in Fig. 8(b). In Fig. 8(c) an estimate of the nucleation rate density is given using values presented in Figs. 8(a) and 8(b). During nucleation and growth it is assumed that crystal positions are random (uncorrelated) and that the small-angle scattering is produced by the crystal form factors [6,10]. The growth process produces a depletion zone around each crystal, and this leads to a maximum in the small-angle scattering at finite wave vector. Model calculations have been made for crystal-depletion zone structures that conserve the total particle number [10] and these give $R = 1.8/q_{1/2}$ as an estimate of crystal size R . If the equilibrium complement of the crystal is realized at t_c and assuming $q_{\min} = 1.8/R_c$ remains valid, then the nucleation rate density N in the coexistence region is given by

$$N = \frac{(\phi - 0.494)/(0.545 - 0.494)}{4\pi R_c^3 t_c / 3}. \quad (4)$$

This is simply the fraction of sample filled with crystal divided by the size of the average crystal and the elapsed time of the measurement.

Recently a classical theory for the nucleation and growth of colloidal crystals has been proposed [9,34] and evaluated numerically (with some modifications) for suspensions of hard spheres [23]. Within this classical theory the critical nucleus size r^* reduced by the particle radius a is given by

$$r^*/a = 8\pi\gamma_{f-s}a^2/3\phi_s(\mu_f - \mu_s), \quad (5)$$

and the free-energy ‘‘barrier to nucleation’’ at this critical size is given by

$$\Delta G(r^*) = (4\pi\gamma_{f-s}a^2/3)(r^*/a)^2. \quad (6)$$

Here the averaged crystal surface tension is given by γ_{f-s} and the difference in chemical potential between the metastable fluid and crystal by $\mu_f - \mu_s$, while the crystal volume fraction is ϕ_s . The chemical potentials and the surface energy are known from computer simulations of hard spheres [13] and analytic calculations [37,36,34]. The nucleation rate density is given by

$$N = \beta[D_s(\phi_f)/a^5]\phi_f^{5/3}\exp[-\Delta G(r^*)/kT], \quad (7)$$

where $D_s(\phi_f)$ is a self-diffusion constant that may be estimated from experiments [34] and β is a parameter expected to be of order unity, although in application of classical theory to atomic systems it may vary from unity by several orders of magnitude [38]. Crystal growth is assumed to follow a Wilson-Frenkel law,

$$dX/d\tau = \delta\{1 - \exp[(\mu_f - \mu_s)/kT]\}, \quad (8)$$

where X is the crystal diameter reduced by the particle radius, $\tau = D_0 t / a^2$ is the reduced time introduced previously, and $\delta = \alpha D_s(\phi_f) / 2D_0$ is a reduced velocity with α an adjustable parameter thought to be of order unity. The self-diffusion constant in the Wilson-Frenkel law need not be identical to the one presented in the nucleation rate density.

The theory is compared with experiment for growth by using the ‘‘known’’ values for the surface tension and chemical potentials, but adjusting the parameter δ so that the size R_c at time t_c agrees with the experimentally observed values. These sizes and times are shown in Fig. 8 for the two different sized particle suspensions. For pure hard spheres δ is a function of volume fraction only, and we find that a fit to the small-particle growth data gives δ values approximately the same (within $\sim 2x$) as those for the larger-particle

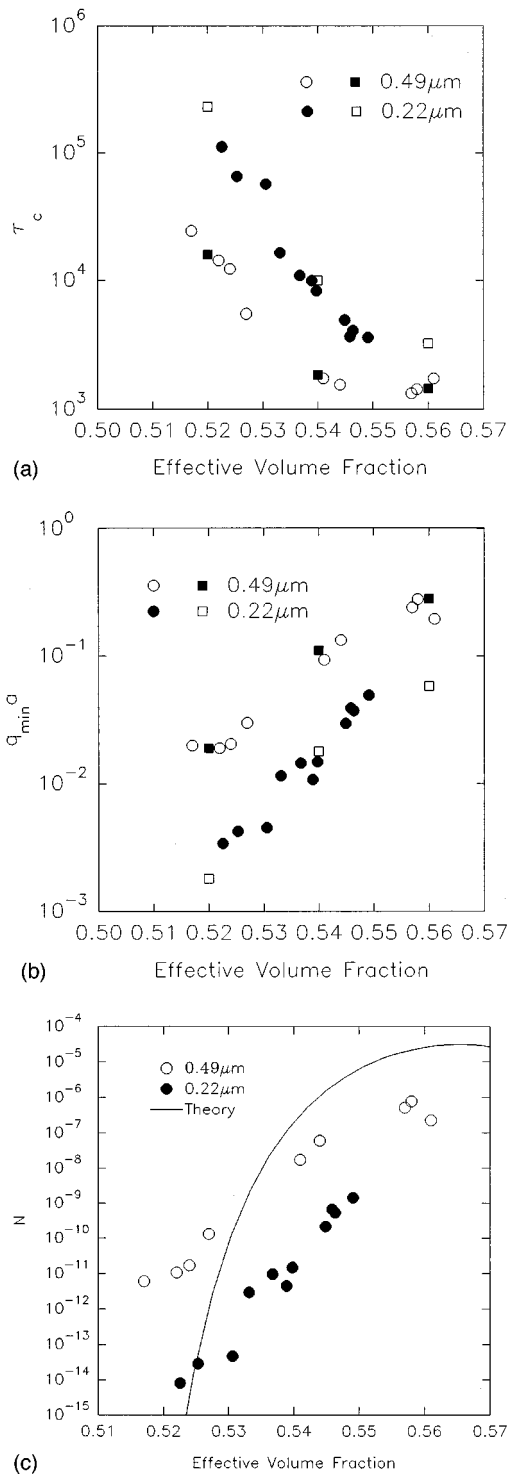


FIG. 8. The elapsed time to the I_m maximum given by Dt_c/a^2 (a), the reduced $q_{1/2}$ minimum given by $q_{\min}^0 a$ (b), and the nucleation rate density given by N (c) as a function of volume fraction for 0.49 μm (\circ) and 0.22 μm (\bullet) radius particles. The solid curve in (c) is the predicted value from classical nucleation theory for hard spheres with $\gamma_{f-s} = 0.16kT/a^2$, $\beta = 1$, and the self-diffusion constant described in the text. The open and solid squares in (a) and (b) at $\phi = 0.52, 0.54$, and 0.56 are from computer simulations with $\delta = 0.1, 0.05$, and 0.004 for the open squares and $\delta = 0.04, 0.026$, and 0.013 for the closed squares, respectively.

samples at the same volume fraction. The reduced nucleation rate density theoretical results are also shown using a form for the self-diffusion constant, $D_s(\phi) = D_0(1 - \phi/0.58)^{1.74}$, given by van Duijneveldt [34] and assuming β is unity. Clearly the two different particle sizes give different results, and the theory could fit either (but not both) equally well if one has complete freedom to adjust β . The theory shows a much stronger dependence on volume fraction than the data as the freezing point is approached.

The source of the discrepancies between the two different particle size systems merits further comment. While it has been claimed that these particle systems are close approximations of hard-sphere systems, it has also been argued that the stabilizing layer introduces some “softness” into the interaction that becomes more important as the ratio of the stabilizing layer thickness to the particle radius increases [18]. The rate of crystallization has been reported to increase in silica particle systems when this ratio is increased [3]. Furthermore, charge stabilized particle suspensions, though at much lower particle volume fraction, have soft interparticle interactions and evidence a rapid crystal growth that is linear in elapsed time to produce rather large crystals [7]. Another indication of softness could be the increase in scaling factor applied to ϕ_w to obtain ϕ as particle size decreases. These observations may lead one to suspect that softer interparticle interactions between the smaller particles are responsible for the observed differences reported above. However, the rate of nucleation is actually slower for the smaller particles [Fig. 8(c)] when scaled to account for particle size. Furthermore, the phase diagram is consistent with that for hard spheres where the coexistence region width is 10% of the freezing value. For softer repulsive potentials the coexistence region is expected to become relatively more narrow [19,20]. Other studies of the width of the coexistence region, which change ratio of stabilizing layer thickness to particle radius for PMMA core particles and a poly(12-hydroxystearic acid) coating, show similar hard-sphere behavior [16]. In addition, low shear viscosity measurements on PMMA particles by Mewis [18] show expected hard-sphere behavior. At large stresses or volume fractions the softness of the interaction may need to be taken into account, but this “softness” does not seem to be important for non-sheared samples undergoing crystallization. We conclude that “soft” interparticle interactions are not the primary cause for the observed differences between the large- and small-particle suspensions.

Another factor that could influence the crystallization properties of the suspensions is the polydispersity. It is measured to be 7% for the small-particle samples and 5% for the larger-particle samples [6]. This is not a large difference but may be significant. As polydispersity increases, both the nucleation rate and the growth rate may be reduced. A single large particle in the presence of small ones can disrupt or delay the formation of a critical nucleus of smaller particles, until the larger particle has diffused out of the way. Similarly, the growth rate is slowed, because not every particle is the right size to fit into the growing front of a crystal. Evidently the self diffusion constants appropriate for nucleation and growth in monodisperse suspensions should be modified to include this slower diffusive process. Polydispersity can also slow the ripening process, because “misfits” are ex-

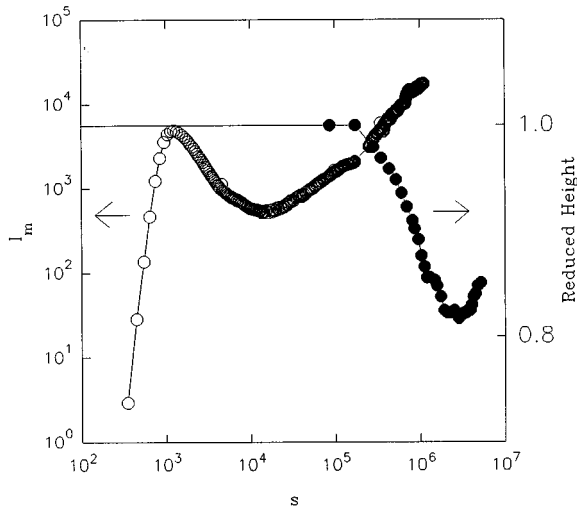


FIG. 9. This plot compares the time evolution of $I_m(t)$ in sample $p4$ with the observed sedimentation. Measurable sedimentation is observed only well into the ripening range.

pelled from crystals into the grain boundaries. These impurities act to pin the boundaries and slow the ripening.

The reduced nucleation rate density noted in Figure 8 for the smaller particle samples are in agreement with these arguments, since the polydispersity is larger for these samples. The larger crystal sizes observed in the smaller-particle samples result from the reduced nucleation rate density, which allows more volume for a crystal to grow into before the onset of ripening. For sufficiently high polydispersities, the order-disorder transition is suppressed [39]. However, in our studies the polydispersity is not sufficiently large to evidence any narrowing of the coexistence region for the smaller-particle samples. Thus we conclude that polydispersity is a candidate for the observed differences measured in the two different size particle samples but a quantitative theory needs development. Evidently polydispersity has no significant influence on the growth rate.

Another difference between the two sample systems is the effect of sedimentation. In dilute suspension the sedimentation velocity is given by the ratio of buoyant weight of the particle to the Stokes' drag [21] and is proportional to the particle radius squared. When sedimentation velocities are scaled by this number, the values obtained depend only on particle volume fraction [12]. Thus the ratio of the sedimentation velocities of the small to the large particles is 0.19, and this fivefold difference is evident in the time taken to characterize the phase diagram for each system (13 d vs 62 d, respectively, from the sedimentation data of large-particle sample $p4$ [6] and small particle sample $p7$, which have almost the same concentration). No measurable sedimentation is observed in these systems until elapsed times corresponding to ripening, as can be seen in Fig. 9. However, at t_c the onset of the crossover region, the samples have probably realized the equilibrium complement of crystal and must simply phase separate over a long period of time into colloidal-liquid and colloidal-crystal-rich regions. For the volume fractions studied (greater than $\phi \sim 0.52$), the samples contain $\sim 50\%$ crystal or more in equilibrium. Assuming uniformly sized spherical particles and placing them at the vertices of a cubic lattice, one finds that the separation be-

tween surfaces of nearest-neighboring particles is less than 2% of their diameter. Thus very little sedimentation is required to achieve large percolation clusters of crystals. These networks would be sensitive to gravitationally induced stresses. Since the gravitational forces on particles are proportional to the buoyant weight, restructuring is expected to occur faster in the larger-particle samples. Indeed, the crossover region is smaller or absent in the larger-particle samples. We believe this is the primary cause of the differences in time to ripening in the two different systems. However, polydispersity could also slow the ripening by trapping "misfits" in the grain boundaries, but the "pinning" of grain boundaries can give a smaller power-law growth behavior than that observed here.

B. Small times

The intensity maximum I_m initially increased, proportional to the fourth power of the elapsed time in the larger-particle systems for volume fractions at and below the melting point. Above the melting point the power-law exponent was difficult to determine because the data were near the noise floor of the apparatus. The exponent appeared to be somewhat less and on the order of 3. For the same time range the characteristic wave vector $q_{1/2}$ showed little measurable change at the largest volume fractions but decreased with a power-law exponent of 0.5 at the melting point and a slightly larger exponent at the smallest volume fractions studied. These exponents suggested a diffusion-limited growth process in contrast to the linear growth observed in charge stabilized particle suspensions [2]. A simple crystal growth model was introduced to explain these data [5,10]. It was assumed that randomly positioned single crystals and associated depletion zones produced the small-angle scattering. The magnitude of the scattering is proportional to the sixth power of the crystal size times the number of scatterers. This size is proportional to the reciprocal of the characteristic wave vector and a constant rate of nucleation is assumed. With these assumptions one finds

$$I_m \sim q_{1/2}^{-6} t \sim t^{6\alpha+1}, \quad (9)$$

where α is the exponent characterizing the time dependence of the wave vector. For $\alpha=0.5$ the growth exponent for the intensity is 4.0, as observed [6].

For the small-particle samples the growth exponents for I_m are found to be larger, being 4.66 at $\phi=0.531$, increasing to a maximum of 7.15 at $\phi=0.545$, and then decreasing to 5.75 at the melting point. The noise floor limited accurate determination of growth exponents for $\phi > 0.552$, which appeared smaller (~ 3.3) than that determined at the melting point. The characteristic wave-vector exponents α were also found to be larger, approximately 0.75 at lower volume fractions up to 1.01 at the melting point.

To determine the validity of the model summarized by Eq. (9), we plot the intensity growth exponent and $6\alpha+1$ as a function of volume fraction in Fig. 10. At the lower volume fractions these exponents agree with the model, suggesting a constant nucleation rate, as assumed previously for the larger-particle systems. Near melting, however, the exponents differ by order unity, indicating only an initial burst of

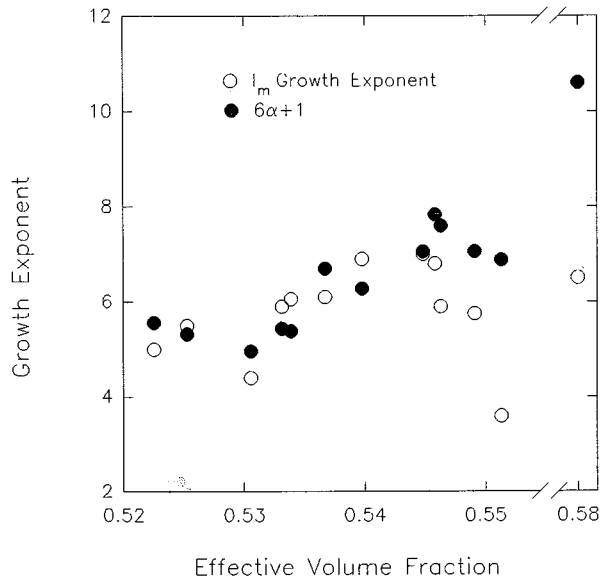


FIG. 10. Intensity growth exponent (○) and $6\alpha+1$ (●) as a function of volume fractions.

nuclei. This has also been suggested as an explanation for the behavior of the largest volume fraction of the larger-particle samples [6].

A range of exponents similar to those measured for α has been observed recently [23] in calculations of crystal growth based on the classical theory of nucleation and growth adapted to suspensions of hard spheres [9]. In these calculations the volume fraction and the speed with which particles become incorporated into the growing crystal determine whether the growth is diffusion limited ($\alpha=0.5$), interface limited ($\alpha=1.0$), or has an approximate power-law behavior with an intermediate exponent. For growth in the coexistence region with a large incorporation rate, the growth is diffusion limited with $\alpha=0.5$. For smaller incorporation rates the growth is slower and not diffusion limited. The growth evolves as an approximate power law with exponent $\alpha>0.5$. Thus the slower growth of the smaller-particle samples (due to polydispersity?) is consistent with the larger growth exponents. The maximum growth exponents we found in our model calculations for the smaller-hard-sphere-particle suspensions were for $\phi=0.52$, from $\alpha=0.58$ at $\delta=0.5$ to $\alpha=0.74$ at $\delta=0.05$; for $\phi=0.54$, $\alpha=0.75$ at $\delta=0.05$; and for $\phi=0.56$, $\alpha=0.55$ at $\delta=0.005$. With increasing volume fraction, the growth exponent increases slightly as do the experimental data. However, for volume fractions greater than freezing, the theoretical value is much reduced from unity, due to finite-size effects. The growth never has time to approach the limiting value because of competition with neighboring crystals for metastable fluid.

The crossover region for the smaller-particle samples is similar for all volume fractions studied in the coexistence and fully crystalline phases. At the beginning of the crossover, the intensity maximum I_m decreases with increased elapsed time, while $q_{1/2}$ increases in value, indicating a decrease in the characteristic length scale. The same behavior is observed for the larger-particle samples for volume fractions less than approximately 0.54. However, for volume fractions at or above melting in the larger-radii-particle systems, I_m exhibited a brief inflection and no decrease in value with

increasing elapsed time. Correspondingly, $q_{1/2}$ became constant before decreasing again in the ripening region. The shape function evidenced deviations from the early and late elapsed time forms similar to that shown in Fig. 6. Given the relationship between scattered intensity and characteristic length scale in Eq. (9), the decrease in scattered intensity would seem to correlate with the observed decrease in characteristic length scale. For the smaller volume fraction samples ($\phi<0.535$), the intensity maximum I_m and $q_{1/2}$ reverse directions at the same time (t_c). However, as the concentration of crystals becomes large enough that depletion zones overlap, the proposed scattering mechanism for the nucleation and growth region is corrupted. This is suggested for volume fractions $\phi>0.535$ by the fact that the intensity maximum I_m begins its decrease before $q_{1/2}$ reaches its minimum (largest characteristic length). Thus we picture independent, spatially uncorrelated nuclei to form and grow initially; but as the sample fills with crystals and depletion zones overlap and control the growth of crystals, the crystals become spatially correlated. The crossover region represents the change from a length scale correlated with the “size” of individual crystals to a length scale correlated with the “separation” between neighboring crystals. Since the crystals are in contact in the ripening region, the latter length scale is also a measure of crystal “size.”

Bragg scattering from the first-order peak has been monitored during the crystallization process for a similar hard-sphere suspension [40]. This method works best for volume fractions at melting or larger due to the large number of crystallites scattering to the diode array detector. The small-angle scattering works better for smaller volume fractions where there is increased scattered intensity due to increased crystal size, in general. Thus the two methods complement one another. The integrated intensity of the Bragg peak X is a measure of the crystal fraction. It shows a rapid increase with exponent $\mu=3$ at volume fraction $\phi=0.530$ and exponent $\mu=4$ at volume fraction $\phi=0.548$ followed by a saturation or very slow increase. The reduced times for this change in behavior correlate well with the reduced time in Fig. 8. The argument given in Eq. (9) should be modified for Bragg scattering to read $X\sim t^{3\alpha+1}$ if the nucleation rate is assumed constant. The growth exponents then become $\alpha=0.66$ and 1.0 for volume fractions $\phi=0.530$ and 0.548, where we found via SALS $\alpha=0.63$ and $\alpha=1.0$, respectively. This interpretation gives the same growth exponents determined by both methods. If the peak width is used as a measure of the crystal size, then the growth exponents are half the values cited above and the nucleation rate increases approximately with the square of the elapsed time. However, it is in this volume fraction range that these growth-law measurements are the least reliable in the Bragg scattering method. Also, the Bragg measurements detect only those crystal planes that are oriented to scatter to the detector, while SALS is sensitive to the whole crystal structure. These planes may grow differently than the crystal as a whole. Finally we note that the saturation of X above t_c indicates that crystallization is completed by this time and this assumption leading to Eq. (4) is valid.

C. Late times

The extended crossover region for the small-particle samples has limited our ability to characterize the ripening

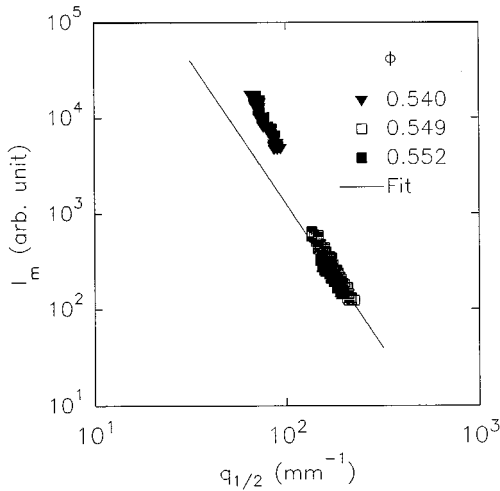


FIG. 11. Peak intensity $I_m(t)$ as a function of characteristic scattering vector $q_{1/2}$ in ripening region. The linear fit shows a slope of -3 (line), which is expected for dynamical scaling in three dimensions.

region. For three samples ($\phi=0.540, 0.549, 0.552$) data runs have been extended to more than two weeks. In the last week, I_m approaches a nearly linear increase with elapsed time, while $q_{1/2}$ decreases with a power law near one-third. This is similar to the behavior observed in the larger-particle samples at the melting point. It may be understood [5] as a ripening process where nearly equilibrium values of liquid and crystal are present, but larger crystals grow at the expense of smaller ones. For example, if the characteristic crystal size is R , then the scattering intensity for a single crystal will go like R^6 , the number of scatterers like R^{-3} , and the total scattered intensity as R^3 . This total intensity increases linearly in time if $q_{1/2}^{-1} \sim R \sim t^{1/3}$. The growth exponent equal to $1/3$ is common in coarsening processes, especially where the order parameter is conserved (known as Lifshitz-Slyozov ripening [24]). Crystallization is described by a nonconserved order parameter, but evidently, the small-angle scattering and the crystallization process are controlled by a conserved quantity, the particle density. In contrast with the larger-particle samples this growth exponent extends into the fully crystalline region (volume fraction 0.552). In the fully crystalline region the larger-particle samples evidenced a larger exponent ($\sim 1/2$) that may increase further with increasing volume fraction. This larger exponent might be expected in fully crystalline samples (Lifshitz-Allen-Cahn behavior [25]).

D. Scaling and dynamical scaling

Dynamical scaling is often observed [26–30] in nonequilibrium phase transformations or coarsening processes. At sufficiently large times the scattered intensity distribution is given by

$$I(q,t) = q_{1/2}^{-d}(t) F[q/q_{1/2}(t)], \quad (10)$$

where d is the dimensionality of the system and F is a shape function. In Fig. 11, the measured peak intensity I_m is plotted as a function of the corresponding characteristic scattering vector $q_{1/2}$ value in the ripening region for sample volume fractions 0.540, 0.549, and 0.552. The limited data for each

sample are compared with the solid line representing a power-law behavior with exponent 3.0. All samples measured show reasonable agreement with an exponent corresponding to three-dimensional space. While larger-particle samples showed the same dynamical scaling in the coexistence region and near the melting point, the exponent was close to 2.0 for the largest volume fractions. This exponent value remains unexplained.

The shape functions do not have universal form but depend on the underlying physical process. General arguments [17] give $F \sim q^2$ as the small wave-vector limit for scattering from conserved quantities like particle density. On the other hand, the large-wave-vector behavior for spinodal decomposition [31,32] is expected [17] to go as $F \sim q^{-4}$ due to well-defined surfaces and scattering in the Porod limit [33]. In electrorheological fluids [35] the large-wave-vector behavior goes as $F \sim q^{-3}$ due to Porod scattering from essentially two-dimensional objects. For irreversible aggregation processes [30], the large-wave-vector limit goes as q^{-d_f} due to the fractal dimension d_f of the scattering clusters. In our samples we expect the small-wave-vector behavior $F \sim q^2$; however, due to the large characteristic size in the ripening region we could not confirm this behavior with the present apparatus. The large-wave-vector behavior suggests $F \sim q^\beta$ where $1 < \beta < 4$. We believe this results from scattering from a polydisperse collection of crystallites. The polydispersity increases with increasing volume fraction but grows self-similarly at a given volume fraction. We do not have a theoretical model for the crystal size distribution but note that the classical theory of nucleation predicts a lower barrier to nucleation as the volume fraction (undercooling) of the metastable state increases. This lower barrier is conducive to a more polydisperse or broader distribution of nucleus sizes.

In the nucleation and growth time regime, the lower volume fraction samples evidence a more complex behavior in the large- Q' portion of the intensity distribution, as seen in Fig. 7. When the data are fit near the maximum intensity with $\gamma \sim 4.0$ in the Furukawa function, it is clear that a smaller exponent is needed to fit the largest Q' intensities. Preliminary microscopy studies for these lower volume fraction samples indicate that there is some substructure within the crystals [22]. Thus, this complex intensity distribution may indicate both scattering from crystals (near the maximum) and from the substructure (for the high- Q' tail). In the crossover and ripening regions this complex behavior is eliminated. Because this transformation is accompanied by a decrease in the characteristic length as noted for Fig. 5, it is natural to suggest that the crystals are breaking up into the smaller substructures. The breakup may result from gravitational stresses or dissolution of crystal at internal defects. The computer calculations [23] of crystal growth indicate that these crystals should be compressed to higher than equilibrium osmotic pressures so internal stresses are expected to be present.

ACKNOWLEDGMENTS

B.J.A. and K.S. were supported by a grant from the North Atlantic Treaty Organization. B.J.A. and Y.H. gratefully acknowledge support from the National Science Foundation through Grant Nos. DMR 9122589 and DMR 9501865.

- [1] S. Brauer, H. E. Fischer, J. O. Ström-Olsen, M. Sutton, and A. Zaluska, *Phys. Rev. B* **47**, 11 757 (1993).
- [2] D. J. W. Aastuen, N. A. Clark, J. C. Swindal, and C. D. Muzny, *Phase Transitions* **21**, 139 (1990).
- [3] C. Smits, J. S. van Duijneveldt, J. K. G. Dhont, H. N. W. Lekkerkerker, and W. J. Briels, *Phase Transitions* **21**, 157 (1990).
- [4] J. K. G. Dhont, C. Smits, and H. N. W. Lekkerkerker, *J. Colloid Interface Sci.* **152**, 386 (1992).
- [5] K. Schätzel and B. J. Ackerson, *Phys. Rev. Lett.* **68**, 337 (1992).
- [6] K. Schätzel and B. J. Ackerson, *Phys. Rev. E* **48**, 3766 (1993).
- [7] D. J. W. Aastuen, N. A. Clark, L. K. Cotter, and B. J. Ackerson, *Phys. Rev. Lett.* **57**, 1733 (1986); **57**, 2772 (1986).
- [8] B. J. Ackerson and N. A. Clark, *Phys. Rev. Lett.* **46**, 123 (1981).
- [9] W. B. Russel, *Phase Transitions* **21**, 127 (1990).
- [10] B. J. Ackerson and K. Schätzel, in *Complex Fluids*, edited by L. Garrido (Springer, Heidelberg, 1992), p. 15.
- [11] L. Antl, J. W. Goodwin, R. D. Hill, R. H. Ottewill, S. M. Owens, S. Papworth, and J. A. Waters, *Colloids Surf.* **17**, 67 (1986).
- [12] S. E. Paulin and B. J. Ackerson, *Phys. Rev. Lett.* **64**, 2663 (1990).
- [13] W. G. Hoover and F. H. Ree, *J. Chem. Phys.* **49**, 3609 (1968).
- [14] P. N. Pusey and W. van Megen, *Nature (London)* **320**, 340 (1986).
- [15] B. J. Ackerson, *J. Rheol.* **34**, 553 (1990).
- [16] S. M. Underwood, J. R. Taylor, and W. van Megen, *Langmuir* **10**, 3550 (1994).
- [17] H. Furukawa, *Physica A* **123**, 497 (1984).
- [18] J. Mewis, W. J. Frith, T. A. Strivens, and W. B. Russel, *AIChE J.* **35**, 415 (1989).
- [19] S. Paulin, B. J. Ackerson and M. S. Wolfe, *J. Colloid Interface Sci.* **178**, 251 (1996).
- [20] J. D. Weeks, *Phys. Rev. B* **24**, 1530 (1981).
- [21] T. G. M. van de Venn, *Colloidal Hydrodynamics* (Academic, New York, 1989).
- [22] Y. He, B. J. Ackerson and B. Olivier (unpublished).
- [23] B. J. Ackerson and K. Schätzel, *Phys. Rev. E* **52**, 6448 (1995).
- [24] I. M. Lifshitz and V. V. Slyozov, *J. Phys. Chem. Solids* **19**, 35 (1965).
- [25] S. M. Allen and J. W. Cahn, *Acta Metall.* **27**, 1085 (1979).
- [26] P. A. Rikvold and J. D. Gunton, *Phys. Rev. Lett.* **49**, 286 (1982).
- [27] J. L. Lebowitz, J. Marro, and M. H. Kalos, *Acta Metall.* **30**, 297 (1982).
- [28] T. Hashimoto, M. Itakura, and H. Hasegawa, *J. Chem. Phys.* **85**, 6118 (1986).
- [29] P. Wiltzius and A. Cumming, *Phys. Rev. Lett.* **66**, 3000 (1991).
- [30] M. Carpineti and M. Giglio, *Phys. Rev. Lett.* **68**, 3327 (1992).
- [31] Y. C. Chou and W. I. Goldburg, *Phys. Rev. A* **23**, 858 (1981).
- [32] C. M. Knobler and N. C. Wong, *J. Phys. Chem.* **85**, 1972 (1981).
- [33] G. Porod, in *Small Angle X-Ray Scattering*, edited by O. Glatter and O. Kratky (Academic, New York, 1982).
- [34] J. S. van Duijneveldt and H. N. W. Lekkerkerker, in *Science and Technology of Crystal Growth*, edited by J. P. van der Eerden and O. S. L. Bruinsma (Kluwer Academic, Dordrecht, 1995).
- [35] J. E. Martin, J. Odinek, and T. C. Halsey, *Phys. Rev. E* **50**, 3263 (1994).
- [36] D. W. Marr and A. P. Gast, *Phys. Rev. E* **47**, 1212 (1993).
- [37] W. A. Curtin, *J. Chem. Phys.* **39**, 6775 (1989).
- [38] K. F. Kelton, *Solid State Phys.* **45**, 71 (1991).
- [39] P. N. Pusey, in *Liquids, Freezing and the Glass Transition*, edited by D. Levesque, J. P. Hansen, and J. Zinn-Justin (Elsevier, Amsterdam, 1990).
- [40] J. Harland, S. Henderson, S. Underwood, and W. van Megen, *Phys. Rev. Lett.* **75**, 3572 (1995).